A Generalized NURBS Framework with Globally G^2 continuity

Yibo Kou
School of Mathematical Sciences, UCAS
Beijing 101408, China
kouyibo21@mails.ucas.ac.cn

Xin Li
School of Mathematical Sciences, USTC
Hefei 230026, China
lixustc@ustc.edu.cn

Ma Hong-yu
School of Mathematical Sciences, UCAS
Beijing 101408, China
mahongyu@ucas.ac.cn

Li Yong Shen
School of Mathematical Sciences, UCAS
Beijing 101408, China
lyshen@ucas.ac.cn

Chun-Ming Yuan
KLMM, AMSS
Chinese Academy of Sciences
Beijing 100190, China
cmyuan@mmrc.iss.ac.cn

Abstract

This paper proposes a method for constructing globally G^2 continuous spline surfaces over control meshes with Extraordinary Points (EPs). For each control mesh face not adjacent to EPs, a bi-cubic Bézier patch is generated, while patches within the 1-ring neighborhood of EPs are subdivided into four sub-patches, each assigned a bi-quintic Bézier patch. Furthermore, we introduce a novel auxiliary control point (anchor) scheme exclusively for sharp EPs to fundamentally overcome the inherent deficiency of G-NURBS in accurately modeling sharp features at singular points. G^2 continuity conditions are enforced at shared patch boundaries by optimizing the positions of Bézier control points. Experimental results not only validate the method's effectiveness in achieving global G^2 continuity near EPs but also, through comparative studies with existing methods, demonstrate its superior geometric fidelity and high-accuracy reconstruction of CAD models containing sharp features. The hybrid patch configuration, combined with a stepwise optimization strategy and the enhanced sharp feature modeling capability, effectively addresses continuity and fidelity challenges arising from arbitrary topological meshes.

***Keywords:* Extraordinary points, G^2 continuity, G-NURBS, fitting.**

1. Introduction

Subdivision surfaces (e.g., Catmull-Clark) and NURBS dominate geometric modeling, yet their incompatibility remains a longstanding challenge. Subdivision surfaces excels in representing smooth surfaces of arbitrary topology but lacks NURBS' precision and compatibility with CAD workflows. While NURBS has become the de facto standard in CAD/CAM due to its parametric precision and compatibility with engineering pipelines, its inherent reliance on rectangular control grid topology fundamentally prohibits the representation of extraordinary points (EPs). Previous patch-based methods attempted to address the issue of G^1 continuous surface generation at EPs [3, 4, 9]. Recent research has proposed a method called G-NURBS [1], which generates globally G^1 continuous spline surfaces on control meshes containing EPs. However, G^1 continuity still falls short of the smoothness requirements for certain high-precision applications, especially in fields such as automotive and aerospace engineering, where even subtle artifacts can be unacceptable.

While significant progress has been made in constructing curvature-continuous spline surfaces, existing approaches that achieve formal G^2 continuity remain limited in scope. Early theoretical analysis [2] established the theoretical feasibility of G^2 continuity using bi-quintic patches, yet practical constructions require more elaborate frameworks. Subsequent works achieved high-quality G^2 surfaces via bi-6 single-patch caps [7] or bi-5 2×2 macro-patches guided by auxiliary surfaces [5]. The method by Loop and Schaefer [15] fills an n-sided hole in a Catmull-Clark spline ring using nbiseptic patches. However, a key limitation of this and similar prior approaches is their assumption that EPs are isolated by regular regions, preventing the handling of adjacent EPs, which is a common scenario in complex CAD models. Scaffold-specific constructions [6] are further restricted to minimal single-valence (MSV) meshes with uni-

form EP valence, while the T-gon-focused splines of [8] address a different class of irregularities related to mesh density transitions rather than EPs and do not achieve formal G^2 continuity. Moreover, none of these methods support the explicit modeling of sharp geometric features at EPs, which are essential for industrial reverse engineering. In contrast, our approach achieves global G^2 continuity on arbitrary topology control meshes, specifically overcoming key limitations of prior works. Our method not only handles adjacent EPs but also introduces an auxiliary anchor point scheme for high-fidelity sharp feature reconstruction, addressing challenges their frameworks do not support.

Building on the success of G-NURBS, this paper introduces the next step in the evolution of spline surfaces by proposing a G^2 continuous version of the method. The key difference in our approach lies in achieving G^2 continuity across the entire surface, including at irregular patches around EPs. G^2 continuity is indispensable in industrial design and engineering, where even minor curvature discontinuities can compromise both functionality and aesthetics. In automotive and aerospace applications, for instance, surfaces with G^2 continuity ensure stress distribution accuracy in finite element analysis and aerodynamic efficiency in computational fluid dynamics. Similarly, consumer product design demands flawless reflection lines (e.g., smartphone casings, luxury car bodies), which are unattainable with G^1-only surfaces. The absence of curvature jumps also eliminates machining vibrations in CNC toolpaths, directly enhancing manufacturing precision. Thus, G^2 continuity bridges the gap between CAD aesthetics and CAE reliability, which is a dual requirement unmet by prior methods.

In the original G-NURBS framework, each control mesh face is initially represented as a bi-cubic Bézier patch, with irregular patches (adjacent to EPs) subsequently elevated to single bi-quintic Bézier patches. These patches enforce G^1 continuity across spoke edges (the boundary curves radiating from an EP) through blending functions, while maintaining C^1 continuity with regular regions. However, this single-patch formulation inherently limits curvature continuity due to insufficient degrees of freedom (DoFs).

Our method advances the original G-NURBS framework through two critical modifications. First, each irregular patch adjacent to an EP is replaced by a 2×2 array of bi-quintic Bézier patches, expanding the local degrees of freedom (DoFs). This topological refinement enables explicit control over curvature variations across spoke edges. Second, we reformulate the blending functions along spoke edges by introducing G^2-compatible connection constraints between adjacent irregular patches. Specifically, the coefficients of these blending functions are analytically derived to enforce G^2 continuity along spoken edges and C^2 continuity elsewhere. This dual strategy resolves the under-constrained nature of single patch G-NURBS formulations, where limited DoFs prevented curvature coherence.

The spline surfaces generated under the proposed framework exhibit lossless forward and backward compatibility with industry-standard NURBS, ensuring seamless interoperability within existing CAD workflows. This bidirectional compatibility preserves geometric fidelity during both data import and export, eliminating conversion-induced artifacts or precision degradation.

However, even after achieving the desired G^2 continuity, a fundamental limitation persists in original G-NURBS or active G-NURBS frameworks when dealing with the strictly sharp geometric features common in industrial CAD and reverse engineering. The surface geometry around sharp features, particularly where the variation of the normal vector near the EP occurs, is crucial for the CAM process as it significantly impacts the toolpath generation quality [16]. The inherent construction of the basis functions restricts the localized geometric expressive power at the EPs. This constraint prevents high-accuracy feature-preserving surface reconstruction from fully meeting industrial demands regarding both the precision and geometric form of sharp corners. Therefore, addressing this localized modeling deficiency is identified as the second critical challenge for achieving industrial-grade, high-fidelity surface reconstruction.

Building on the establishment of global G^2 continuity, we introduce another critical modification aimed at local feature fidelity. A novel auxiliary control point scheme is incorporated exclusively at sharp EPs. This point acts as a degree of freedom in the optimization, fundamentally resolving the inherent expressive deficiencies of G-NURBS for sharp features. This advancement enables unprecedented accuracy in feature-preserving surface reconstruction, ensuring that the final G-NURBS surface maintains both global G^2 smoothness and localized sharp corner fidelity.

In summary, the main contributions of this work are:

- A generalized NURBS framework that achieves global G^2 continuity over arbitrary topology control meshes, including configurations with adjacent extraordinary points, thereby extending the original G^1 G-NURBS to a higher-order smoothness regime.
- An analytically derived set of G^2 continuity constraints along spoke edges, combined with a stepwise optimization strategy that decouples the solution for isolated and adjacent EPs, effectively resolving the under-constrained nature of single-patch formulations and preventing excessive global coupling.
- A novel auxiliary control point (anchor) scheme at sharp extraordinary points, which enables high-fidelity reconstruction of sharp geometric features while preserving global G^2 continuity, thereby addressing a

long-standing limitation of original G-NURBS in industrial reverse engineering.

The remainder of this paper is structured as follows: Section 2 details the guidance surface construction methodology for control meshes with extraordinary points (EPs). Section 3 formulates the G² continuity conditions and their reformulation as linear constraints on the Bézier coefficients along both sides of spoke edges. Section 4 presents the comprehensive framework for constructing G^2 continuous surfaces and demonstrates the results of the proposed hybrid-degree Bézier framework, validating G^2 continuity. Section 5 demonstrates applications in industrial surface modeling and reconstruction, highlighting the method's superiority in handling sharp features. Finally, Section 6 discusses limitations of the current approach and outlines future directions for solution stability and computational acceleration.

2. Guidance surface

Similar to the original G-NURBS framework, the proposed method first constructs a guidance surface via a generalized Bézier extraction technique [1]. This surface, while only C^0-continuous at spoke edges near extraordinary points (EPs), serves as a geometrically meaningful initial configuration to guide subsequent continuity optimizations. Although the guidance surface itself does not satisfy G^2 continuity requirements, its topology-aware shape provides a robust initialization for optimizing Bézier control points, thereby steering the global geometry toward G^2 continuity around EPs. Continuity constraints are then systematically imposed on spoke edges to refine the Bézier patches' boundary alignment and curvature coherence.

The following delineates the workflow of the generalized Bézier extraction procedure, which enables the generation of a bi-cubic Bézier surface patch per face on control meshes containing extraordinary points (EPs). The Bézier extraction process is implemented through stepwise linear interpolation of the original control points, sequentially generating three distinct control point categories: face points, edge points, and vertex points.

Each bi-cubic Bézier patch comprises 16 control points, which can be categorized into three distinct types based on their geometric arrangement within the patch. Four of these points, termed face points, occupy the central area of the surface patch, while eight edge points are situated at the mid-edge positions along each of the four boundaries. The remaining four control points, designated as vertex points, reside precisely at the four corner locations of the patch, forming a spatial hierarchy essential to the patch's geometric representation. As shown in Fig. 1, the symbols F_i, E_i, and V_i correspond to face points, edge points, and vertex points within the control mesh topology, respectively.

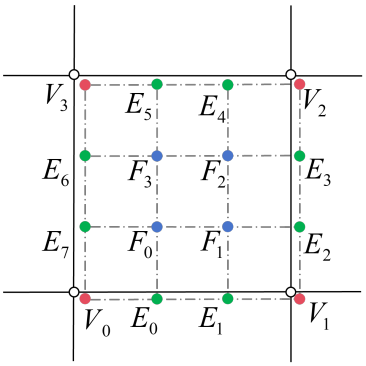

Figure 1. The 16 control points of each bi-cubic Bézier patch are classified into three categories. Blue points represent face points, green points denote edge points, and red points indicate vertex points. Solid black lines depict the input control mesh edges while dashed lines illustrate the 4×4 control grid of the bi-cubic Bézier patch.

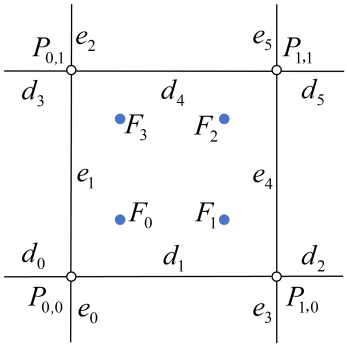

Figure 2. The face points are extracted based on the four vertices of the corresponding control mesh face and the associated knot intervals along each edge.

As illustrated in Fig. 2, where $P_{i,j}(i,j=0,1)$ represent the control points on the mesh and $e_i, d_i(i=0,\ldots,5)$ denote the knot intervals assigned to the corresponding edges of the control mesh.

The face points $F_{2j+i}(i,j=0,1)$ of each Bézier patch are computed through a weighted averaging of its adjacent control points and knot interval parameters.

$$\begin{aligned} F_{2j+i} =&(1-\alpha_{i,j})[(1-\gamma_{i,j})P_{0,0}+\gamma_{i,j}P_{0,1}] \\ &+\alpha_{i,j}[(1-\gamma_{i,j})P_{1,0}+\gamma_{i,j}P_{1,1}], \end{aligned}$$

where

$$\alpha_{0,j}=\frac{h_0^j}{h_0^j+h_1^j+h_2^j}, \alpha_{1,j}=\frac{h_0^j+h_1^j}{h_0^j+h_1^j+h_2^j},$$
$$\gamma_{i,0}=\frac{k_0^i}{k_0^i+k_1^i+k_2^i}, \gamma_{i,1}=\frac{k_0^i+k_1^i}{k_0^i+k_1^i+k_2^i},$$

with

$$h_n^j = \frac{(2-j)d_n + (1+j)d_{n+3}}{3},$$
$$k_n^i = \frac{(2-i)e_n + (1+i)e_{n+3}}{3}.$$

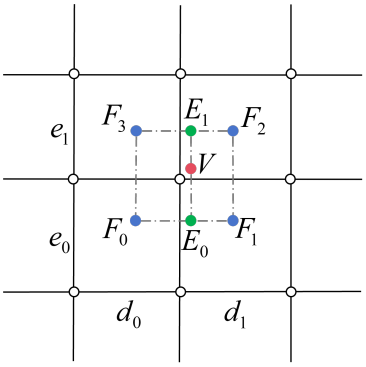

Figure 3. Edge points are computed through knot-interval-based linear interpolation between adjacent face points. Vertex points are similarly derived by interpolating between connected edge points. Dashed lines indicate these interpolation relationships, where line weights correspond to knot interval values.

Following the computation of face points, the edge points E_i and vertex points V are subsequently derived through linear combination of their adjacent face points, as illustrated in Fig. 3. For regular patches, the specific expressions are

$$E_0 = \frac{d_1F_0 + d_0F_1}{d_0 + d_1}, V = \frac{e_1E_0 + e_0E_1}{e_0 + e_1}. \quad (1)$$

For irregular patches, the computation of edge points follows the same procedure as defined in Eq. (1), while vertex points are formulated as linear combinations of adjacent face points across neighboring surface patches. This configuration is demonstrated in Fig. 4, where a vertex point V associated with a valence N EP is expressed through

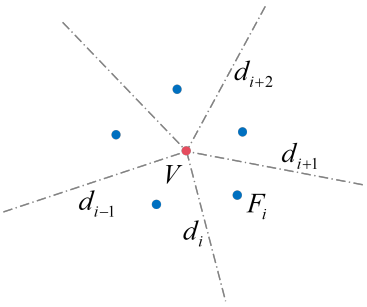

Figure 4. The vertex point at a valence EP is computed through a weighted combination of the nearest face points from the N surrounding irregular patches.

$$V = \frac{\sum_{i=1}^{N} \alpha_i F_i}{\sum_{i=1}^{N} \alpha_i}, \quad (2)$$

where $\alpha_i = d_{i-1}d_{i+2}$.

After Bézier extraction, each face of the control mesh is associated with a corresponding bi-cubic Bézier surface patch. As inherently guaranteed by the Bézier extraction procedure, the resulting spline surface satisfies C^2 continuity outside the 1-ring neighborhoods of EPs. Consequently, the bi-cubic Bézier patches within the irregular regions (i.e., EP 1-ring neighborhoods) undergo degree elevation and subdivision to introduce sufficient degrees of freedom for subsequent enforcement of G^2 continuity constraints. Here, each irregular Bézier patch $S(u, v)$ is intrinsically partitioned at the parametric coordinates $u = 0.5$ and $v = 0.5$. Following this process of degree elevation and surface subdivision, the number of Bézier control points per irregular patch increases from 36 to 121, establishing an expanded control grid that accommodates the enforcement of G^2 continuity across patch boundaries.

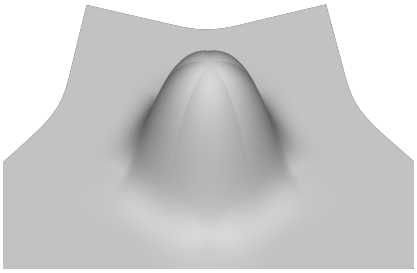

Figure 5. The guidance surface constructed on a control mesh containing a valence five EP exhibits C^2 continuity outside the EP's one-ring neighborhood, while maintaining C^0 continuity between adjacent irregular patches.

The final quadrilateral control mesh generates an initial guidance surface composed of bi-cubic Bézier patches in regular regions and a 2×2 array of bi-quintic Bézier patches within irregular regions. Fig. 5 demonstrates a control mesh containing a valence 5 EP and its associated guidance surface. The resulting surface preserves C^2 continuity across all regions exterior to the 1-ring neighborhoods of the EP.

Subsequent steps enforce G^2 continuity constraints along spoke edges by optimizing the control points of these irregular bi-quintic patches to achieve curvature-compatible transitions between adjacent sub-patches and the surrounding bi-cubic regions.

3. Constraints for G^2continuity

3.1. G^2 Conditions

G^2 continuity between adjacent Bézier patches requires the alignment of first-order, second-order and mixed partial derivatives across their shared boundary. This condition is mathematically enforced through connection functions.

Consider two adjacent irregular Bézier surface patches, denoted as $A(s, t)$ and $B(s, t)$, within a guidance sur-

face. The two patches share a common boundary curve $R(s) = A(s,0) = B(s,0)$. These patches are G^2 continuous along $R(s)$ if and only if there exist functions $\alpha(s), \beta(s), \gamma(s), \delta(s)$ and $\rho(s)$ defined over R(s) such that the following conditions hold:

$$\alpha(s)B_t(s,0) + \gamma(s)A_t(s,0) = \beta(s)A_s(s,0), \tag{3}$$

$$\begin{aligned}\alpha^2(s)B_{tt} - \gamma^2(s)A_{tt}\big|_{(s,0)} &= \delta(s)A_s + \rho(s)\gamma(s)A_t \\ &\quad - 2\beta(s)\gamma(s)A_{st} \\ &\quad + \beta^2(s)A_{ss}\big|_{(s,0)},\end{aligned} \tag{4}$$

where Eq. (3) establishes G^1 continuity by enforcing coincident tangent planes at the patch boundary, while the additional Eq. (4) guarantees G^2 continuity.

In our setting, $\alpha(s)$ and $\gamma(s)$ are constants, which are denoted as α and γ respectively. Differentiating both sides of Eq. (3) with respect to s, we obtain

$$\alpha B_{st}(s,0) + \gamma A_{st}(s,0) = \beta(s)A_{ss}(s,0) + \beta'(s)A_s(s,0)$$

which leads

$$\begin{aligned}\beta^2(s)A_{ss}(s,0) =& \alpha\beta(s)B_{st}(s,0) + \gamma\beta(s)A_{st}(s,0) \\ &- \beta(s)\beta'(s)A_t(s,0)\end{aligned} \tag{5}$$

Subscribing the above Eq. (5) into Eq. (4), the right side of Eq. (4) equals to

$$\begin{aligned}&-\beta(s)\gamma A_{st}(s,0) + \alpha\beta(s)B_{st}(s,0) + \\ &\frac{\delta(s) - \beta(s)\beta'(s)}{\beta(s)}\left(\gamma A_t(s,0) + \alpha B_t(s,0)\right) + \rho(s)\gamma A_t(s,0).\end{aligned}$$

In the G^1 continuous G-NURBS framework, only Eq. (3) is required, where the partial derivatives of adjacent Bézier patches $A(s,t)$ and $B(s,t)$ in the t-direction exhibit formal symmetry. However, under G^2 continuity conditions, this symmetry breaks down. Analytical and empirical observations reveal that the t-directional partial derivatives of Bézier patches $A(s,t)$ and $B(s,t)$ in Eq. (4) lack symmetry. Direct application of Eq. (4) as a G^2 continuity constraint introduces structural asymmetry in the Bézier control points on both sides of spoke edges that are governed by these partial derivatives. This asymmetry propagating to the G-NURBS basis functions during the solution process and manifests as unintended curvature distortion in the final surface geometry, particularly near extraordinary points. Fig. 6 demonstrates the consequences of omitting formal symmetry constraints on the partial derivatives in Eq. (4). Even after implementing global optimization on the Bézier control points within the 1-ring neighborhood of the EP, the resulting control points distributions exhibit undesirable warping characteristics.

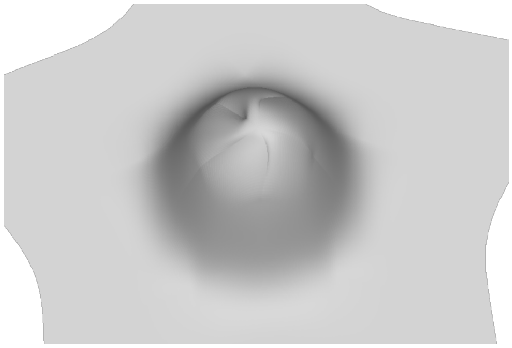

Figure 6. The solution process propagates asymmetry into the G-NURBS basis functions, resulting in unintended curvature distortion in the final surface geometry. This effect is particularly pronounced near the EP.

To constructively enforce coefficient symmetry between $A_t(s,0)$ and $B_t(s,0)$, we define the connecting functions via the relation

$$\frac{\delta(s) - \beta(s)\beta'(s)}{\beta(s)} + \rho(s) = -\frac{\delta(s) - \beta(s)\beta'(s)}{\beta(s)}, \tag{6}$$

which gives

$$\delta(s) = \beta(s)\beta'(s) - \frac{1}{2}\beta(s)\rho(s)$$

This equality inherently arises from the geometric duality of $A_t(s,0)$ and $B_t(s,0)$ along their shared boundary.
Let

$$W(s) = \gamma A_t(s,0) - \alpha B_t(s,0), \tag{7}$$

then Eq. (4) turns to be

$$\frac{1}{2}\rho(s)W(s) - \beta(s)W'(s) = \alpha^2 B_{tt}(s,0) - \gamma^2 A_{tt}(s,0). \tag{8}$$

And then, $A_t(s,0)$ and $B_t(s,0)$ can be solved according to Eq. (3) and Eq. (7)

$$A_t(s,0) = \frac{\beta(s)A_s(s,0) + W(s)}{2}, \tag{9}$$

$$B_t(s,0) = \frac{\beta(s)A_s(s,0) - W(s)}{2}, \tag{10}$$

where $W(s)$ must satisfy the constraint of Eq. (8).

3.2. Deriving G^2 Constraints on Spoke Edges

Now we study the G^2 condition and provide a solution for optimizing the Bézier control points of n irregular patches with knot intervals d_i. Each irregular patch is represented with 2 × 2 bi-quintic Bézier patches and other regular patches are bi-cubic Bézier representation. We first study the G^2 continuity for the i-th spoke edge and then provide the basic framework to construct the entire G^2 G-NURBS surface. The construction methodology diverges

between isolated and adjacent EPs, necessitating separate elaborations for these two topological configurations in the subsequent analysis.

3.2.1 An EP connects with a regular points

Fig. 7 illustrates a case where the two end vertices of a spoke edge are an EP and a regular point. In this case, the gray Bézier control points are computed from the adjacent bi-cubic patches with C^2 continuity. Since the guidance surface generated by Bézier extraction maintains C^2 continuity along the connecting edges between regular and irregular patches, the gray control points can be directly obtained through degree elevation and subdivision of the bi-cubic Bézier surface control points. And the black Bézier

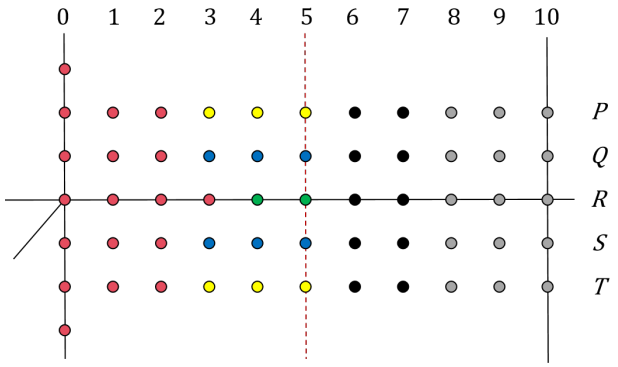

Figure 7. G^2 continuity for a spoke edge with only one EP.

control points can be defined through the C^2 continuous for the red line, which satisfy the following equations

$$\begin{cases} X_3 - 2X_4 + X_5 = X_5 - 2X_6 + X_7, \\ X_4 - X_5 = X_5 - X_6, \end{cases} \tag{11}$$

in which X stands for P, Q, R, S, T. So we only need study the G^2 continuous for Bézier control points P_j, Q_j, R_j, S_j, T_j for $j = 0, \ldots, 5$.

For the G^2 continuity, we assume that

$$\begin{aligned} &\alpha = \gamma = 1, \\ &\rho(s) = r_i(1-s)^3, \\ &\beta(s) = b_i(1-s)^3, \end{aligned}$$

where $r_i = 1$ and b_i employs the same computation method as used in G^1 G-NURBS, which is based on eigen-polyhedron [14].

For $j = 0, \ldots, 5$, denote

$$\begin{aligned} K_j &= \frac{Q_j - R_j}{d_{i+1}} - \frac{S_j - R_j}{d_{i-1}}, \\ V_j &= \frac{T_j - 2S_j + R_j}{d_{i-1}^2} - \frac{P_j - 2Q_j + R_j}{d_{i+1}^2}, \end{aligned}$$

where we can observe that $V_3 = V_4 = V_5 = 0$.

If we write $\alpha^2 B_{tt}(s,0) - \gamma^2 A_{tt}(s,0)$ with Bézier form, which is quintic, it has the form of

$$20\left\langle V_0, V_1, V_2, 0, 0, 0\right\rangle = 20(1-s)^3 \left\langle V_0, \frac{5}{2}V_1, 10V2 \right\rangle,$$

where $\langle\rangle$ denotes the Bézier coefficients of some degrees. And then Eq. (8) is

$$\frac{r_i}{2}W(s) - b_i W'(s) = 20\left\langle V_0, \frac{5}{2}V_1, 10V2 \right\rangle.$$

From above equation, we can conclude that $W(s)$ is quadratic, which is denoted as $\langle W0, W1, W2\rangle$.

On the other hand, $W(s)$ can also be written into a quintic Bézier form with control points

$$50\left\langle K_0, K_1, K_2, K_3, K_4, K_5\right\rangle.$$

According to the degree elevation, we can conclude that $5\left\langle K_0, K_1, K_2, K_3, K_4, K_5\right\rangle$ equals to

$$\begin{aligned} \Big\langle & W_0,\ \frac{3}{5}W_0 + \frac{2}{5}W_1,\ \frac{3}{10}W_0 + \frac{3}{5}W_1 + \frac{1}{10}W_2, \\ & \frac{3}{10}W_2 + \frac{3}{5}W_1 + \frac{1}{10}W_0,\ \frac{3}{5}W_2 + \frac{2}{5}W_1,\ W_2 \Big\rangle, \end{aligned}$$

which leads

$$\begin{aligned} W_0 &= 5K_0, \\ W_1 &= \frac{5}{2}(5K_1 - 3K_0), \\ W_2 &= 50K_2 - 75K_1 + 30K_0. \end{aligned}$$

Thus, $K_i (i = 3, 4, 5)$ are linear combination of K_0, K_1 and K_2,

$$\begin{aligned} K_3 &= K_0 - 3K_1 + 3K_2, \\ K_4 &= 3K_0 - 8K_1 + 6K_2, \\ K_5 &= 6K_0 - 15K_1 + 10K_2. \end{aligned}$$

Now we will write these constrains in terms of Q_i, R_i and $S_i (i = 3, 4, 5)$ according to Eq. (9) and Eq. (10),

$$\begin{cases} Q_3 = R_3 + \dfrac{d_{i+1}}{2}\left(K_0 - 3K_1 + 3K_2\right), \\ S_3 = R_3 - \dfrac{d_{i-1}}{2}\left(K_0 - 3K_1 + 3K_2\right), \\ Q_4 = R_4 + \dfrac{d_{i+1}}{2}\left(3K_0 - 8K_1 + 6K_2\right), \\ S_4 = R_4 - \dfrac{d_{i-1}}{2}\left(3K_0 - 8K_1 + 6K_2\right), \\ Q_5 = R_5 + \dfrac{d_{i+1}}{2}\left(6K_0 - 15K_1 + 10K_2\right), \\ S_5 = R_5 - \dfrac{d_{i-1}}{2}\left(6K_0 - 15K_1 + 10K_2\right). \end{cases} \tag{12}$$

As R_i is degree elevation of a cubic curve $\langle A_0, A_1, A_2, A_3\rangle$, then

$$\begin{aligned}
A_0 &= R_0,\\
A_1 &= \frac{5R_1}{3} - \frac{2R_0}{3},\\
A_2 &= \frac{10R_2}{3} - \frac{10R_1}{3} + R_0,\\
A_3 &= 10R_3 - 20R_2 + 15R_1 - 4R_0,
\end{aligned}$$

which can lead

$$\begin{cases}
R_4 = 4R_3 - 6R_2 + 4R_1 - R_0,\\
R_5 = 10R_3 - 20R_2 + 15R_1 - 4R_0.
\end{cases} \tag{13}$$

Thus, we can observe that the blue control points are linear combination of the red ones.

However, the red control points are not totally freely to choose, they must satisfy some more constrains, where

$$\begin{cases}
V_0 = \frac{r_i}{40}W_0 - \frac{b_i}{10d_i}(W_1 - W_0)\\
\quad = \frac{r_i}{8}K_0 - \frac{5b_i}{4d_i}(K_1 - K_0),\\
V_1 = \frac{r_i}{100}W_1 - \frac{b_i}{50d_i}(W_2 - W_0)\\
\quad = \frac{r_i}{40}(5K_1 - 3K_0) - \frac{b_i}{2d_i}(2K_2 - 3K_1 + K_0),\\
V_2 = \frac{r_i}{400}W_2 - \frac{b_i}{100d_i}(W_2 - W_1)\\
\quad = r_i\left(\frac{K_2}{8} - \frac{3K_1}{16} + \frac{3K_0}{40}\right)\\
\qquad - \frac{b_i}{d_i}\left(\frac{K_2}{2} - \frac{7K_1}{8} + \frac{3K_0}{8}\right).
\end{cases} \tag{14}$$

and

$$\begin{cases}
Q_0 = R_0 + \frac{d_{i+1}K_0}{2} + \frac{d_{i+1}b_i}{d_i}\left(\frac{1}{2}R_1 - \frac{1}{2}R_0\right),\\
Q_1 = R_1 + \frac{d_{i+1}K_1}{2} + \frac{d_{i+1}b_i}{d_i}\left(\frac{2}{5}R_2 - \frac{3}{5}R_1 + \frac{1}{5}R_0\right),\\
Q_2 = R_2 + \frac{d_{i+1}K_2}{2} +\\
\qquad \frac{d_{i+1}b_i}{d_i}\left(\frac{3}{10}R_3 - \frac{7}{10}R_2 + \frac{11}{20}R_1 - \frac{3}{20}R_0\right).
\end{cases} \tag{15}$$

In this context, the control points are assigned distinct colors based on their positions. The red control points represent those associated with the EP, and all G^2 continuity constraints related to the red control points must be satisfied simultaneously. Once the red points are determined, the G^2 continuity constraints corresponding to the green, blue, and yellow control points can be derived. Here, the green, blue, and yellow control points denote the variables governing the zeroth-order, first-order, and second-order continuity, respectively, along the shared boundary of two adjacent patches. The black and gray control points are situated on the patches adjacent to the regular points. After all control points associated with the EP and the shared boundary are determined, the black control points can be directly computed from linear constraints. Subsequently, the gray control points are obtained via Bézier extraction. This process serves to maintain the G^2 continuity with adjacent regular patches.

3.2.2 Two adjacent EPs

When a spoke edge contains two EPs as its endpoints, as depicted in Fig. 8, the Bézier control points within the shared boundary region possess additional degrees of freedom, thereby enabling rigorous enforcement of G^2 continuity constraints. For this spoke edge, we assume

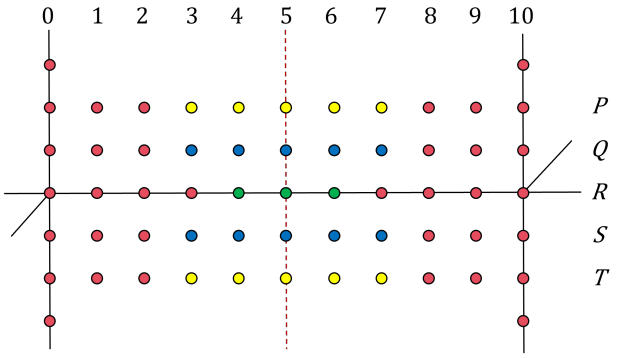

Figure 8. G^2 continuity for a spoke edge with two adjacent EPs.

$$\begin{aligned}
&\alpha = \gamma = 1,\\
&\rho(s) = r_i,\\
&\beta(s) = b_i^1(1-s) - b_i^2 s,
\end{aligned} \tag{16}$$

where $r_i = 1$, $b_i^1 = b_0$ and $b_i^2 = \frac{1}{2}(b_0 + b_1)$. b_0 and b_1 are associated with R_0 and R_{10}, respectively, and are computed via the method in G^1 G-NURBS [1] based on eigen-polyhedron.

Similar as above, we provide all the G^2 constraints. The first part constrains are defined for those green, blue and yellow control points, which are linear combination of the red ones.

First, R_i should be C^3 continuous at $s = 0.5$ since the surface is C^2 along the red line and Eq. (3) has As on the right side. This leads that R_4, R_5 and R_6 can be computed

explicitly.

$$\begin{aligned} R_5 &= \frac{3}{4}R_7 - \frac{1}{4}R_8 + \frac{3}{4}R_3 - \frac{1}{4}R_2, \\ R_4 &= R_5 + \frac{1}{4}R_3 - \frac{1}{4}R_7, \\ R_6 &= R_5 - \frac{1}{4}R_3 + \frac{1}{4}R_7. \end{aligned} \tag{17}$$

Similarly, we can observe that W(s) is also C^3 at s = 0.5 according to equation (6). Thus, if we fix the red control points, then K_3 and K_7 are degrees of freedom and K_4, K_5 and K_6 can be computed explicitly.

$$\begin{aligned} K_5 &= \frac{3}{4}K_7 - \frac{1}{4}K_8 + \frac{3}{4}K_3 - \frac{1}{4}K_2, \\ K_4 &= K_5 + \frac{1}{4}K_3 - \frac{1}{4}K_7, \\ K_6 &= K_5 - \frac{1}{4}K_3 + \frac{1}{4}K_7. \end{aligned}$$

After fix $W(s)$, then the only constrains for yellow control points are Eq. (8). All above equations are used for optimizing the control points for edges.

For those red control points, the constraints are those conditions in Eq. (3) and Eq. (8).

Similar to the G^1 G-NURBS case, $\alpha^2 B_{tt}(s,0) - \gamma^2 A_t t(s,0)$ and $W(s)$ can be denoted as $20\langle V_0, V_1, V_2, V_3, V_4, V_5\rangle$ and $5\langle K_0, K_1, K_2, K_3, K_4, K_5\rangle$ respectively, then we can write down the constraints according to Eq. (3) and Eq. (8). First we write down the constraints for those red control points,

$$\begin{cases} Q_0 = R_0 + \frac{d_{i+1}}{2}K_0 + \frac{d_{i+1}b_i^1}{2d_i}(R_1 - R_0), \\ Q_1 = R_1 + \frac{d_{i+1}}{2}K_1 + \frac{2d_{i+1}b_i^1}{5d_i}(R_2 - R_1) \\ \qquad + \frac{d_{i+1}b_i^2}{10d_i}(R_1 - R_0), \\ Q_2 = R_2 + \frac{d_{i+1}}{2}K_2 + \frac{3d_{i+1}b_i^1}{10d_i}(R_3 - R_2) \\ \qquad + \frac{d_{i+1}b_i^2}{5d_i}(R_2 - R_1), \\ V_0 = \frac{r_i}{8}K_0 - \frac{5}{4}b_i^1(K_1 - K_0), \\ V_1 = \frac{r_i}{8}K_1 - \frac{4}{4}b_i^1(K_2 - K_1) - \frac{1}{4}b_i^2(K_1 - K_0), \\ V_2 = \frac{r_i}{8}K_2 - \frac{3}{4}b_i^1(K_3 - K_2) - \frac{2}{4}b_i^2(K_2 - K_1). \end{cases} \tag{18}$$

After getting the red control points, blue points can be directly computed by the following equations.

$$\begin{cases} Q_3 = R_3 + \frac{d_{i+1}}{2}K_3 + \frac{d_{i+1}b_i^1}{5d_i}(R_4 - R_3) \\ \qquad + \frac{3d_{i+1}b_i^2}{10d_i}(R_3 - R_2), \\ Q_4 = R_4 + \frac{d_{i+1}}{2}K_4 + \frac{d_{i+1}b_i^1}{10d_i}(R_5 - R_4) \\ \qquad + \frac{2d_{i+1}b_i^2}{5d_i}(R_4 - R_3), \\ Q_5 = R_5 + \frac{d_{i+1}}{2}K_5 + \frac{d_{i+1}b_i^2}{2d_i}(R_5 - R_4), \\ S_3 = R_3 - \frac{d_{i-1}}{2}K_3 + \frac{d_{i-1}b_i^1}{5d_i}(R_4 - R_3) \\ \qquad + \frac{3d_{i-1}b_i^2}{10d_i}(R_3 - R_2), \\ S_4 = R_4 - \frac{d_{i-1}}{2}K_4 + \frac{d_{i-1}b_i^1}{10d_i}(R_5 - R_4) \\ \qquad + \frac{2d_{i-1}b_i^2}{5d_i}(R_4 - R_3), \\ S_5 = R_5 - \frac{d_{i-1}}{2}K_5 + \frac{d_{i-1}b_i^2}{2d_i}(R_5 - R_4). \end{cases} \tag{19}$$

Finally, optimize yellow points under below constrains.

$$\begin{cases} V_3 = \frac{r_i}{8}K_3 - \frac{2}{4}b_i^1(K_4 - K_3) - \frac{3}{4}b_i^2(K_3 - K_2), \\ V_4 = \frac{r_i}{8}K_4 - \frac{1}{4}b_i^1(K_5 - K_4) - \frac{4}{4}b_i^2(K_4 - K_3), \\ V_5 = \frac{r_i}{8}K_5 - \frac{5}{4}b_i^2(K_5 - K_4). \end{cases} \tag{20}$$

In the case of adjacent EPs, the control points of different colors and their meanings refer to the scenario of an isolated EP as described in Sec 3.2.1.

4. Optimization of G^2 Basis Functions

In Sec 3, we transform the G^2 continuity conditions into linear constraints on Bézier control points, encompassing both cases of adjacent EPs and isolated EPs on spoke edges. These constraints are all imposed on the three peripheral rows of control points in the Bézier patch that are directly related to G^2 continuity. We now present the complete construction framework for building G^2 continuous basis functions on irregular patches.

4.1. Fundamental Construction Framework

First, as demonstrated in Sec2, bi-cubic Bézier patches are obtained through Bézier extraction. For irregular patches, the bi-cubic surface is converted into a 2×2 bi-quintic patch through degree elevation and split. This operation preserves the original shape of the guidance surface while introducing additional Bézier control points to

provide the necessary degrees of freedom for subsequent G^2 continuity constraints. The Bézier control points are then adjusted by solving a constrained optimization problem, yielding G^2 continuous G-NURBS surface. Below, we elaborate on the precise formulation and stepwise solution process of this optimization problem.

For the case of isolated EP on the spoke edge, the following procedure is adopted to optimize the Bézier coefficients.

4.1.1 Optimize red, green and blue coefficients of an isolated EP simultaneously

The corresponding coefficients in Fig. 7 are uniformly denoted as $U_{i,j}$, where (i, j) denotes the grid indices of control points, with i and j representing the row and column positions respectively in the Bézier patch. The difference vector $C^s_{i,j}$ and $C^h_{i,j}$ of $U_{i,j}$ are given by

$$\begin{aligned} C^s_{i,j} &= U_{i,j} - U_{i,max(j-1,0)}, \\ C^h_{i,j} &= U_{i,j} - U_{max(i-1,0),j}. \end{aligned}$$

All $U_{i,j}$ are aggregated into vector U, while all $C^s_{i,j}$ and $C^h_{i,j}$ form vector C. Correspondingly, let $\widetilde{U}$ and $\widetilde{C}$ represent the coefficients and their differences obtained directly from the original Bézier surface through degree elevation and split operations. Obtaining the red, green, and blue coefficients in this step can be formulated as solving a linearly-constrained optimization problem

$$\begin{aligned} \min_{U} \quad & \|U - \widetilde{U}\|_2^2 + \|C - \widetilde{C}\|_2^2, \\ \text{s.t.} \quad & M_I U = 0, \end{aligned} \tag{21}$$

where the linear constraints are given by Eq. (12), Eq. (13), Eq. (14) and Eq. (15). It should be noted that for an isolated EP of degree N, the red, green, and blue coefficients associated with all N spoke edges must be optimized simultaneously to prevent asymmetry in the G^2 G-NURBS basis functions.

Building upon this foundation, the black coefficients can be directly determined through the C^2 continuity constraints expressed in Eq. (11). The gray coefficients are directly assigned the values obtained by degree elevation and split of the bi-cubic coefficients.

4.1.2 Optimize yellow coefficients of an isolated EP

Once the red, green, and blue coefficients are determined, the yellow coefficients along each spoke edge connected to the isolated EP can be optimized independently. The optimization minimizes the deviation between these yellow coefficients and their corresponding values derived from the guidance surface after degree elevation and split. In this phase, the yellow coefficients need only satisfy three G^2 continuity conditions. This completes the G^2 continuity optimization between adjacent patches along each spoken edge. The corresponding optimization problem is formulated as

$$\begin{aligned} \min_{P_i, T_i} \quad & \sum_{i=3}^{5} \|P_i - \widetilde{P}_i\|_2^2 + \|T_i - \widetilde{T}_i\|_2^2, \\ \text{s.t.} \quad & P_i - 2Q_i = T_i - 2S_i, i = 3, 4, 5, \end{aligned} \tag{22}$$

where $\widetilde{P}_i$ and $\widetilde{T}_i$ represent the corresponding coefficients on the guidance surface.

4.1.3 Optimize central coefficients of an isolated EP

With all coefficients affecting G^2 continuity with adjacent Bézier patches (i.e., the three peripheral rows of coefficients) already determined for the irregular patch, we now address the remaining 25 central coefficients. These interior coefficients are obtained by minimizing the thin-plate energy

$$E_s = \iint \left(\left\| \tilde{S}_{uu} \right\|^2 + 2 \left\| \tilde{S}_{uv} \right\|^2 + \left\| \tilde{S}_{vv} \right\|^2 \right) \mathrm{d}u \, \mathrm{d}v.$$

This minimization produces a surface with minimal bending energy while maintaining C^2 continuity constraints between the 2×2 sub-patches generated through splitting of the irregular patch. The complete optimization problem can be formulated as

$$\begin{aligned} \min \quad & E_s(L), \\ \text{s.t.} \quad & M_C L = 0, \end{aligned}$$

where L denotes the vector composed of 25 central coefficients and the linear constraints $M_C L = 0$ follow a formulation similar to that specified in Eq. (11).

For spoke edges containing two adjacent EPs, we employ a distinct optimization framework from that used for isolated EP to prevent excessive computational complexity in the resulting optimization problem.

4.1.4 Optimize red coefficients of two adjacent EPs

For EPs on both sides of a spoke edge, we first independently optimize the red coefficients surrounding each EP. The objective function follows a formulation analogous to Eq. (21), while explicitly excluding the green and blue coefficients from consideration. The constraint conditions prescribed in Eq. (18) must be satisfied simultaneously.

4.1.5 Optimize green, blue and yellow coefficients of two adjacent EPs

With the red coefficients fixed, the green and blue coefficients can be directly computed according to Eq. (17) and

Eq. (19). Subsequently, the green coefficients on both sides of each spoke edge can be optimized independently through a method similar to Eq. (22), while satisfying the constraints specified in Eq. (20).

Following the optimization of all coefficients governing G^2 continuity at patch boundaries, the remaining 25 interior coefficients are determined using the same methodology as for isolated EPs. For cases involving adjacent EPs, the aforementioned localized optimization framework enables separate computation of coefficients surrounding EPs at both ends of each spoke. This approach ensures independent determination of yellow coefficients across different spoke edges. Such a stepwise optimization strategy effectively prevents excessive complexity in the global optimization problem that would otherwise arise from contiguous EPs in the control mesh.

4.2. Computational Complexity Analysis

The computational cost of the proposed optimization framework primarily depends on the number of EPs m and their respective valences $k_i (i = 1, \ldots, m)$.

The core optimization process, formulated in Equations (21) and (22), involves solving a sequence of constrained least-squares problems. For each EP of valence k, the size of the optimization problem for its surrounding 2×2 bi-quintic Bézier patches scales linearly with k, as the number of control points and G^2 constraints along each spoke edge is fixed. Crucially, the employed stepwise optimization strategy decouples the global problem into manageable sub-problems. Specifically, the coefficients for EPs are optimized first, followed by independent optimizations for the coefficients along each spoke edge. This approach prevents the formation of a single, large globally-coupled system that would have $O(\sum_{i=1}^{m} k_i)$ variables, which could become prohibitively expensive for complex meshes.

The overall computational cost of the stepwise solution method can be formulated as

$$\mathcal{C}_{\text{total}} = \sum_{i=1}^{m} \mathcal{C}(O(k_i)),$$

where $\mathcal{C}(\cdot)$ denotes the computational complexity of solving a constrained least-squares problem, which depends on the specific algorithm employed. Typically, $\mathcal{C}(n)$ grows superlinearly with the number of variables n. The stepwise optimization strategy effectively decouples the global problem into independent small-scale sub-problems for each EP, thereby significantly reducing the overall surface generation cost.

4.3. Result

We now present the visualization results of our proposed G² G-NURBS framework to demonstrate its efficacy. We first present a G^2 continuous G-NURBS surface generated from a control mesh containing a valence five EP.

Fig. 9 demonstrates the continuity control and surface quality around the EP using reflection lines and Gaussian curvature visualization, which illustrate smooth light flow transition and depict the intrinsic curvature distribution, respectively, both indicating excellent continuity and local shape quality. This result demonstrate that our proposed framework successfully generates well-shaped G^2 continuous surface. This example further illustrates the morphology of the spline basis functions generated by our algorithm at the EP. Notably, under centrally symmetric control meshes, the algorithm produces G^2 continuous basis function that preserve geometric symmetry. When compared with the results in Fig. 6, this clearly validates the effectiveness of our symmetry-preserving approach through the connection functions defined in Eq. (6).

Fig. 10 presents an additional case featuring a valence eight EP. Even under this extreme configuration, our method successfully generates a spline surface with both satisfactory global morphology and guaranteed G^2 continuity. This result substantiates that the proposed framework imposes no strict upper bound on EP's valence and demonstrates robust capability in handling complex scenarios involving varying EP degrees within control meshes.

We now present additional numerical examples to demonstrate both the efficacy and generality of our proposed algorithm.

The results in Fig. 11 and Fig.12 further demonstrate that our method generates well-behaved G^2 continuous surfaces across diverse input meshes containing EPs. The reflection lines confirm the superior smoothness of the G^2 G-NURBS surfaces. Fig. 13 presents additional G^2 G-NURBS surfaces along with their corresponding control meshes.

5. Application

This section is dedicated to demonstrating the practical utility of our proposed Globally G^2 continuous G-NURBS framework across two crucial domains: geometric modeling and surface reconstruction. The G^2 G-NURBS paradigm not only provides a robust solution for guaranteeing high-order continuity over arbitrary topologies but, critically, offers superior geometric control, especially for the precise representation of sharp features.

5.1. Accurate construction of sharp features in CAD surface modeling

The construction principle of G-NURBS is fundamentally based on modifying the continuity of adjacent Bézier patches at their common boundaries by enforcing geometric continuity constraints. By adjusting the continuity between the patches, this inherent flexibility enables the creation of sharp features across the surface, including both

(a) Control mesh with an EP (b) G^2 G-NURBS surface (c) Reflection lines (d) Gaussian curvature

Figure 9. G^2 G-NURBS surface of the control mesh with an EP.

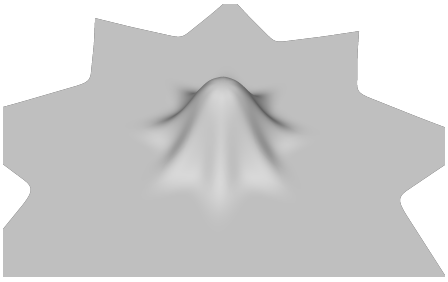

Figure 10. G^2 G-NURBS surface of the control mesh with a valence eight EP.

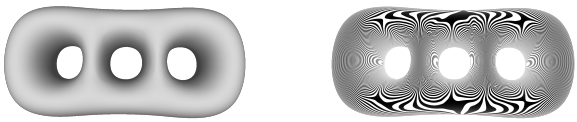

(a) G^2 G-NURBS surface with three holes. (b) Reflection lines

Figure 11. The G^2 G-NURBS surface with three holes.

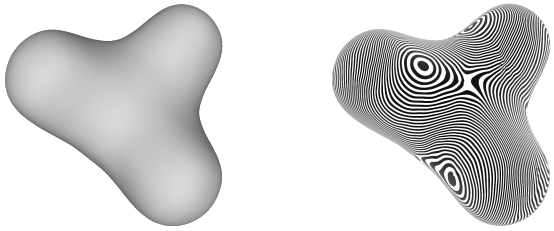

(a) G^2 G-NURBS surface. (b) Reflection lines

Figure 12. G^2 G-NURBS surface and its corresponding reflection lines.

global and local characteristics. This is particularly effective for features traversing EPs. We first exploit this specific property of G^2 G-NURBS as the foundation for defining C^0 sharp features on the surface. Building upon this, we introduce a novel auxiliary control point, which we term the anchor, specifically at the EPs traversed by the sharp feature. This critical addition substantially augments the G^2 G-NURBS's fine-grained control over local geometric information, thereby enabling a more precise and accurate representation of sharp features.

As can be observed from the core mathematical formulation of the G-NURBS construction process described in Section 2, the foundational guidance surface is rigorously derived through the Bézier extraction procedure. This critical initial step fundamentally operates by performing a linear interpolation of the positional coordinates of the vertices in the input control mesh to determine the precise control points for the set of C^0 continuous Bézier patches. This process, while guaranteeing global C^0 continuity, inherently dictates the base geometric configuration.

Consequently, when a spoke edge (the edge situated adjacent to an EP) is explicitly designated as a sharp edge, a sharp feature can indeed be topologically established at the corresponding location, often one that traverses the EP. However, the exact geometric form and fidelity of this constructed sharp feature remain heavily constrained and influenced by the preceding Bézier extraction process—specifically, they are intrinsically tied to the initial positional information of the vertices in the input control mesh.

This fundamental constraint poses a significant practical challenge in interactive surface modeling design. It renders the construction of corner points that successfully maintain a desired sharp geometric and visual appearance extremely difficult, especially when these critical sharp features pass directly through an EP.

As visually demonstrated in Fig. 14b, even under the most favorable condition where all spoke edges surrounding an EP are systematically designated as sharp edges, the resulting G-NURBS surface, though possessing the required C^0 continuity at the feature line, exhibits a persistent and undesirable tendency toward smoothness in the overall surface geometry adjacent to the corner. Consequently, instead of manifesting the expected salient and prominent sharp corner point typically required in high-fidelity CAD models, the local geometry appears visibly faired or rounded. Crucially, this unsatisfactory geometric phenomenon is not

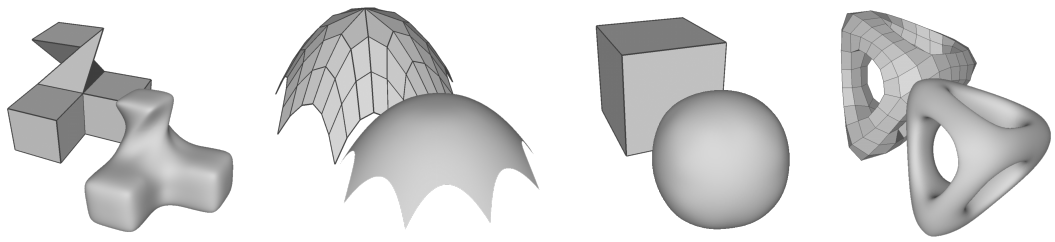

Figure 13. G^2 G-NURBS surfaces and their corresponding control meshes.

effectively mitigated, even when attempting manual interventions, such as the deliberate adjustment or positional stretching of the extraordinary control point at the sharp feature.

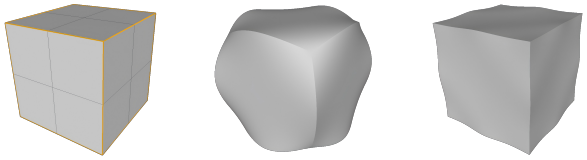

(a) Control mesh. (b) Original G-NURBS (c) Our method

Figure 14. Sharp features constructed by original G-NURBS and our G^2 G-NURBS with anchor at EPs. (a) is a control mesh with designated sharp edges around EPs (highlighted in orange). (b) and (c) are the results of sharp features constructed near EP by the original G-NURBS and the G-NURBS with anchors we added, respectively.

To overcome this critical and inherent limitation of the original G-NURBS construction method regarding the deficient geometric representation of sharp features at EPs, we propose a targeted and novel solution involving the introduction of an auxiliary control point.

The specific technical approach involves a fundamental modification during the crucial Bézier extraction phase. An auxiliary control point, denoted as A_{EP}, is explicitly generated and positioned at the sharp EP location. Consequently, the standard computation for the vertex point V_{EP} on the extraordinary Bézier patch, which typically corresponds to the location of the EP, is fundamentally altered. Instead of relying on the linear interpolation defined by Eq. 2, which often leads to the undesired smoothing, the vertex point V_{EP} is directly and definitively assigned the coordinates of the newly introduced auxiliary control point, such that

$$V_{EP} = A_{EP}. \tag{23}$$

As shown in Fig. 14c, this improvement allows the construction of sharper and geometrically superior features at the sharp corner passing through EP by simply adjusting the position of the anchor points. This targeted modification consequently mitigates, to a significant extent, the inherent geometric deficiency in sharp corner modeling that was previously caused by the Bézier extraction process within the original G-NURBS framework. The direct assignment of the vertex point V_{EP} to the anchor point A_{EP} effectively bypasses the problematic linear averaging, thereby allowing for the creation of a geometrically well-defined and sharp corner feature.

Fundamentally, this modification is mathematically equivalent to introducing an additional basis function that is specifically localized at the sharp EP. The critical consequence of this introduction is that the extraordinary vertex point V_EP at the EP is no longer linearly dependent on the surrounding vertices of the input control mesh that are processed during the Bézier extraction stage, thus granting localized geometric freedom. Furthermore, the position of this novel auxiliary control point A_EP can be explicitly specified according to the precise requirements of the surface modeling task. This capability is analogous, in the language of spline theory, to the introduction of a dedicated spline basis function whose coefficients can be arbitrarily designated, allowing for highly flexible, yet localized, geometric manipulation. In practice, the positioning of anchor points can be adapted to different application scenarios. For interactive design applications, users can manually adjust the anchor positions to achieve precise control over sharp features. In reconstruction tasks (e.g., reverse engineering), the anchor points can be automatically determined through optimization algorithms, such as by minimizing the fitting error between the reconstructed surface and the input data.

With the incorporation of the auxiliary control point, the construction method for G-NURBS at sharp EPs now benefits from a substantially more sophisticated and fine-grained form of geometric expression. This newly acquired geometric precision, therefore, makes the framework highly amenable for direct application to challenging high-accuracy surface reconstruction tasks that critically require the faithful recovery and retention of complex sharp features.

5.2. High-accuracy surface reconstruction

The fundamental task of surface reconstruction aims to recover a continuous, parametric surface representation from discrete input data formats, such as polygon meshes

and dense point clouds. This process constitutes an essential and foundational stage within the critical field of industrial reverse engineering.

Employing G-NURBS for surface fitting offers a substantial advantage, as it yields a reconstructed surface representation that is inherently compatible with industry-standard formats, thereby providing a crucial bridge for seamless integration into existing CAD/CAM systems.

CAD models are typically defined by highly regular and structured geometric forms. Their defining surface characteristics are generally composed of expansive regions of high-order smoothness, punctuated by highly localized areas where the surface normal exhibits abrupt and significant variation, especially within regions containing strictly sharp geometric features.

Consequently, the surface reconstruction of these CAD models inherently necessitates higher standards of accuracy and geometric fidelity. This demanding requirement stems from the fact that subsequent downstream processes, such as engineering simulation, finite element analysis, and precision manufacturing, are profoundly sensitive to errors in normal continuity and sharp changes in the surface normal at geometric feature lines. This dependency, in turn, imposes stringent requirements on the performance and robustness of feature-preserving G-NURBS fitting methodologies. While many existing spline surface fitting methods are capable of adaptive fitting, which minimizes the number of control points under a prescribed error tolerance [10,11,13,18–21], they predominantly focus on global approximation error. Since these methods generally do not impose additional constraints on sharp features, they are more suitable for free-form organic models than for engineered CAD models containing sharp corners, which are prevalent in industrial applications.

The active G-NURBS method [12] skillfully exploits the intrinsic properties of G-NURBS for managing EPs and constructing sharp features, thereby allowing the methodology to achieve a crucial simultaneous optimization that precisely balances the global fitting error with the localized geometric feature error. Furthermore, the parameterization correspondence strategy specifically engineered within this framework for sharp features is highly effective, ensuring, to a great extent, a strict and accurate correspondence between the sharp features present on the fitting G-NURBS surface and those identified within the input data.

However, despite these advancements, this particular methodology is fundamentally constrained by the very same limitation: it suffers from the insufficient expressive capability of the original G-NURBS framework for representing sharp features precisely at EPs, a deficiency that has been thoroughly discussed in Section 5.1.

Recent work such as truncated hierarchical G-NURBS (TH-GNURBS) [17] has advanced adaptive spline fitting on arbitrary-topology meshes by enabling local refinement while preserving G^1 continuity. However, like most generalized spline frameworks, TH-GNURBS assumes globally smooth surfaces and does not support explicit modeling or preservation of sharp geometric features such as creases and corners that commonly occur at EPs in CAD models. Consequently, when applied to industrial parts with sharp features, TH-GNURBS tends to over-smooth these critical features, compromising geometric fidelity. In contrast, our framework not only achieves global G^2 continuity but also introduces an auxiliary control point (anchor) at sharp EPs, enabling precise reconstruction of sharp features without sacrificing smoothness elsewhere.

Following the augmentation of the G-NURBS framework with an auxiliary control point specifically localized at the sharp EP, the resulting surface is formally represented as

$$S(u,v) = \sum_{i=1}^{N} \mathbf{C}_i G_i(u,v) + \sum_{j=1}^{M} \mathbf{A}_j G_j(u,v). \qquad (24)$$

In this representation, $\mathbf{C}_i$ denotes the positional vectors of the standard control mesh vertices and N represents the total number of these primary control points. $\mathbf{A}_j$ represents the positional vectors of the auxiliary control points and M denotes the total count of EPs that are specifically intersected by a sharp feature. Finally, $G_i(u,v)$ and $G_j(u,v)$ represent the respective G-NURBS basis functions associated with the standard control points and the newly introduced auxiliary anchor points, respectively.

It is critical to note that despite the integration of this supplementary and conceptually virtual control point, the fundamental mathematical form of the G-NURBS surface representation remains entirely preserved. It continues to be defined as the sum of products involving the basis functions and their respective coefficient control points. For those EPs that are not intersected by any sharp features, the construction methodology and subsequent application of the G-NURBS framework can entirely adhere to and utilize the principles established in the initially proposed, unmodified framework. This ensures that the global G^2 continuity guaranteed by the original method remains preserved in these smoother regions, while localized modifications are reserved only for the critical sharp EP locations.

Crucially, this preservation of the underlying structure ensures that the final generated G-NURBS surface can still be losslessly converted into the standard industry format of Bézier patches. This maintained compatibility guarantees that the modified framework remains fully compatible, both forward and backward, with existing industrial pipelines and established CAD/CAM systems. Therefore, the robust surface fitting methodology initially proposed within the active G-NURBS framework can be directly and effectively

utilized for the high-fidelity fitting of CAD model data that exhibits prominent sharp features.

The following results exhibit two practical applications of G^2 G-NURBS in CAD-oriented surface reconstruction. The first case demonstrates its proficiency in smooth surface reconstruction, while the second showcases its ability to preserve sharp geometric features. Together, these examples substantiate the framework's comprehensive surface modeling competence across diverse geometric requirements.

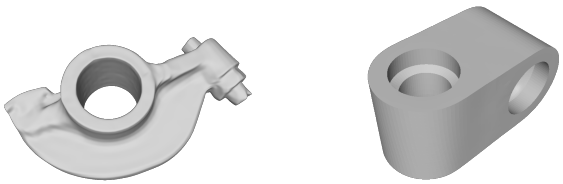

(a) Smooth fitting result of G^2 G-NURBS surface

(b) Fitting result with sharp features of G^2 G-NURBS surface

Figure 15. Two different cases of G^2 G-NURBS fitting.

Furthermore, we provide a comparative visualization of the CAD model fitting results achieved by the proposed auxiliary control point scheme and the original active G-NURBS scheme, as clearly presented in Fig. 16 and Fig. 17. Tab. 1 and Tab. 2 present a comparative summary of the fitting results for the two models respectively. The error metrics are reported as percentages relative to the length of the diagonal of the model's bounding box. Here, d_{max} and d_{avg} denote the global maximum and average fitting errors, while d^f_{max} and d^f_{avg} represent the maximum and average errors specifically within the sharp feature regions of the model. The error comparison demonstrates that the proposed method achieves superior performance in accurately reconstructing sharp geometric features

	Original active G-NURBS	Our method
$d_{max}(\%)$	0.37	0.14
$d_{avg}(\%)$	0.0096	0.0094
$d^f_{max}(\%)$	0.38	0.17
$d^f_{avg}(\%)$	0.045	0.018

Table 1. Statistics of the fitting error for the joint model.

Consequently, based on the comparative results , it is clearly demonstrated that the proposed framework for surface fitting specifically targeting sharp EPs yields significantly superior performance compared to prior art. This inherent advantage directly contributes to a substantial enhancement in the reconstruction quality of CAD models, particularly at regions defined by strictly sharp geometric

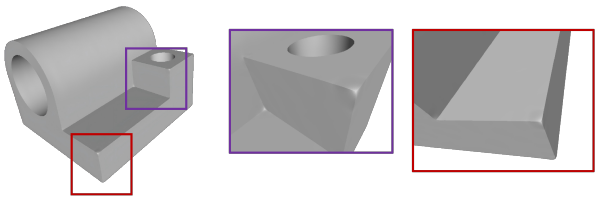

(a) Original active G-NURBS

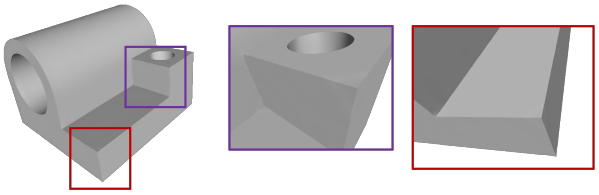

(b) Our method

Figure 16. Comparison of sharp feature fitting results at EP for the joint model.

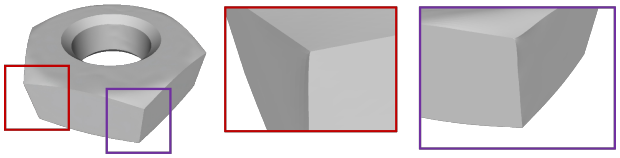

(a) Original active G-NURBS

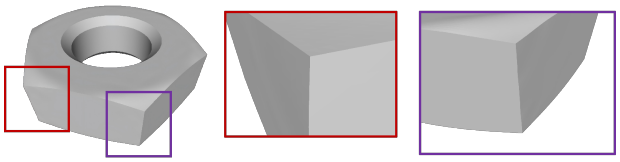

(b) Our method

Figure 17. Comparison of sharp feature fitting results at EP for the nut model.

	Original active G-NURBS	Our method
$d_{max}(\%)$	0.15	0.11
$d_{avg}(\%)$	0.016	0.010
$d^f_{max}(\%)$	0.17	0.13
$d^f_{avg}(\%)$	0.080	0.050

Table 2. Statistics of the fitting error for the nut model.

features. Furthermore, the high fidelity achieved in these critical areas is not merely an aesthetic improvement but further confers a measurable benefit to the precision and reliability of subsequent downstream processes, such as engineering analysis, machining, and manufacturing.

6. Limitations and Future Work

In this paper, we successfully propose a G-NURBS framework capable of constructing spline surfaces with globally G^2 continuity over control meshes of arbitrary topology. We achieved this through a hybrid-degree Bézier patch configuration and a symmetrized G^2 constraint reconstruction scheme, while ensuring lossless compatibility with existing CAD/CAM pipelines.

More significantly, to satisfy the rigorous demands of industrial reverse engineering for strictly sharp geometric features, we further integrated a novel auxiliary control point scheme specifically targeting sharp EPs into our framework. This localized geometric enhancement mechanism effectively overcomes the bottleneck of insufficient modeling capability at singular points inherent in the original G-NURBS framework. Through comparative experiments, we demonstrated that our method achieves high-accuracy, faithful reconstruction of sharp features, even in cases where the original active G-NURBS struggles to provide sufficient geometric accuracy. This capability is vital for enhancing the numerical precision of CAD models at critical features and benefits subsequent manufacturing quality.

Despite these significant advancements, the theoretical guarantee of solution existence and stability for extreme configurations, particularly those involving high-valence EPs or highly irregular knot intervals, requires further theoretical analysis. A promising direction for future research involves refining the optimization problem's solution framework to theoretically guarantee solution existence while maintaining an optimal balance between computational efficiency and numerical accuracy.

Acknowledgement

An acknowledgement is used to thank the person, fund, etc., that support this work.

References

[1] Y.-F. Feng, L.-Y. Shen, X. Li, C.-M. Yuan, and X. Jiang. Patching non-uniform extraordinary points. *IEEE Transactions on Visualization and Computer Graphics*, 30(8):4683–4693, 2024. 1, 3, 7

[2] J. A. Gregory and J. Zhou. Irregular C^2 surface construction using bi-polynomial rectangular patches. *Computer Aided Geometric Design*, 16(5):423–435, 1999. 1

[3] K. Karčiauskas and J. Peters. Low degree splines for locally quad-dominant meshes. *Computer aided geometric design*, 83:101934, 2020. 1

[4] K. Karčiauskas and J. Peters. Bi-cubic scaffold surfaces. *Computer-Aided Design*, 150:103310, 2022. 1

[5] K. Karčiauskas and J. Peters. Biquintic G^2 surfaces via functionals. *Computer Aided Geometric Design*, 33:17–29, 2015. 1

[6] K. Karčiauskas and J. Peters. Curvature continuous bi-4 constructions for scaffold- and sphere-like surfaces. *Computer-Aided Design*, 78:48–59, 2016. SPM 2016. 1

[7] K. Karčiauskas and J. Peters. Minimal bi-6 G^2 completion of bicubic spline surfaces. *Computer Aided Geometric Design*, 41:10–22, 2016. 1

[8] K. Karčiauskas and J. Peters. High quality refinable g-splines for locally quad-dominant meshes with t-gons. *Computer Graphics Forum*, 38(5):151–161, 2019. 2

[9] K. Karčiauskas and J. Peters. Multi-sided completion of C^2 bi-3 and C^1 bi-2 splines: A unifying approach. *Computer Aided Geometric Design*, 86:101978, 2021. 1

[10] T. Kawasaki, P. K. Jayaraman, K. Shida, J. Zheng, and T. Maekawa. An image processing approach to feature-preserving B-spline surface fairing. *Computer-Aided Design*, 99:1–10, 2018. 13

[11] Y. Kineri, M. Wang, H. Lin, and T. Maekawa. B-spline surface fitting by iterative geometric interpolation/approximation algorithms. *Comput. Aided Des.*, 44(7):697–708, July 2012. 13

[12] Y.-B. Kou, Y.-F. Feng, L.-Y. Shen, X. Li, and C.-M. Yuan. Adaptive spline surface fitting with arbitrary topological control mesh. *IEEE Transactions on Visualization and Computer Graphics*, 30(12):7736–7748, 2024. 13

[13] Y.-K. Lai, S.-M. Hu, and H. Pottmann. Surface fitting based on a feature sensitive parametrization. *Computer-Aided Design*, 38(7):800–807, 2006. 13

[14] X. Li, G. T. Finnigan, and T. W. Sederberg. G^1 non-uniform Catmull-Clark surfaces. *ACM Trans. Graph.*, 35(4), July 2016. 6

[15] C. Loop and S. Schaefer. G^2 Tensor Product Splines over Extraordinary Vertices. *Computer Graphics Forum*, 27(5):1373–1382, 2008. 1

[16] H.-Y. Ma, Y.-B. Kou, L.-Y. Shen, and C.-M. Yuan. Efficient tool path planning method of ball-end milling for high quality manufacturing. *Robotics and Computer-Integrated Manufacturing*, 93:102905, 2025. 2

[17] J. Min, X. Li, and L. yong Shen. Truncated hierarchical gnurbs for adaptive spline surface fitting. *Computer-Aided Design*, 189:103928, 2025. 13

[18] H. Park. B-spline surface fitting based on adaptive knot placement using dominant columns. *Computer-Aided Design*, 43(3):258–264, 2011. 13

[19] Y. Wang and J. Zheng. Curvature-guided adaptive t-spline surface fitting. *Computer-Aided Design*, 45(8):1095–1107, 2013. 13

[20] Y. Zhang, J. Cao, Z. Chen, X. Li, and X.-M. Zeng. B-spline surface fitting with knot position optimization. *Computers & Graphics*, 58:73–83, 2016. Shape Modeling International 2016. 13

[21] J. Zheng, Y. Wang, and H. S. Seah. Adaptive t-spline surface fitting to z-map models. In *Proceedings of the 3rd International Conference on Computer Graphics and Interactive Techniques in Australasia and South East Asia*, GRAPHITE '05, page 405–411, New York, NY, USA, 2005. Association for Computing Machinery. 13